Controlled Assembly of Heterobinuclear Sites on Mesoporous Silica: Visible Light Charge-Transfer Units with Selectable Redox Properties

Hongxian Han and Heinz Frei*

Physical Biosciences Division, Lawrence Berkeley National Laboratory

University of California, Berkeley, CA 94720

Abstract

Mild synthetic methods are demonstrated for the selective assembly of oxo-bridged heterobinuclear units of the type $TiOCr^{III}$, $TiOCo^{II}$, and $TiOCe^{III}$ on mesoporous silica support MCM-41. One method takes advantage of the higher acidity and, hence, higher reactivity of titanol compared to silanol OH groups towards Ce^{III} or Co^{II} precursor. The procedure avoids the customary use of strong base. The controlled assembly of the TiOCr system exploits the selective redox reactivity of one metal towards another (Ti^{III} precursor reacting with anchored Cr^{VI} centers). The observed selectivity for linking a metal precursor to an already anchored partner versus formation of isolated centers ranges from a factor of six (TiOCe) to complete (TiOCr, TiOCo). Evidence for oxo bridges and determination of the coordination environment of each metal centers is based on K-edge EXAFS (TiOCr), L-edge absorption spectroscopy (Ce), and XANES measurements (Co, Cr). EPR, optical, FT-Raman and FT-IR spectroscopy furnish additional details on oxidation state and coordination environment of donor and acceptor metal centers. In the case of TiOCr, the integrity of the anchored group upon calcination (350 ^{o}C) and cycling of the Cr oxidation state is demonstrated. The binuclear units possess metal-to-metal charge-transfer transitions that absorb deep in the visible region. The flexible synthetic method for assembling the units opens up the use of visible light charge transfer pumps featuring donor or acceptor metals with selectable redox potential.

1. Introduction

Inert nanoporous oxide materials such as silica offer robust high surface area supports for inorganic polynuclear units for demanding photosynthetic transformations, such as water oxidation or carbon dioxide reduction. Our approach for developing artificial photosynthetic assemblies is based on all-inorganic bi- or polynuclear photocatalytic units arranged and coupled on a nanoporous support, taking advantage of the precision by which one can control energy flow, charge transport and chemical transformations in molecular structures. The nanoporous support affords a means for arranging and coupling of the sites, and the very high surface area allows for sufficient density of photocatalytic units so that the chemistry can keep up with the incident photon flux even at high photolysis light intensity. In addition, the nanostructured features offer ways for ultimately separating reducing from oxidizing catalytic units. With the goal of developing systems driven by solar photons, the principal challenge is to design units that accomplish the oxidation and reduction half reactions with visible instead of UV light. Furthermore, the active groups need to be designed in such a way that reduction and oxidation sites can be coupled under minimal loss of energy or charge.

Our photocatalytic units typically consist of a molecular or well-defined polynuclear multi-electron transfer catalyst coupled to a visible light charge-transfer pump. These pumps are oxo-bridged heterobinuclear moieties, are covalently anchored on the silica nanopore surface, and possess a metal-to-metal charge-transfer (MMCT) absorption covering a large fraction of the visible spectrum.[1] We have recently reported several such binuclear MMCT units in mesoporous silica type MCM-41 ($TiOCu^{I}$,[1]

$TiOSn^{II}$,[1] $ZrOCu^{I}$,[2] $TiOCo^{II}$ [3]) and demonstrated photo-induced CO_2 splitting to CO inside the mesopores for the $ZrOCu^{I}$ system.[2] Nakamura *et al.* have expanded the systems to $TiOCe^{III}$ and demonstrated stability of the unit when utilizing the charge-transfer chromophore for photocatalytic hydrocarbon oxidation.[4] These examples provide proof-of-existence for visible light absorbing charge-transfer units on silica nanopore surfaces consisting of two different metal centers with no ligands other than bridging or siloxy oxygens. Furthermore, the free selection of pairs of metals and oxidation states offers the flexibility required for optimizing visible light absorption properties and, most importantly, for tuning the redox potentials of the donor and acceptor metal centers so as to drive the linked oxidation or reduction catalysts efficiently. Adjustment of the potentials of the metal centers is an essential requirement for minimizing energy losses while accomplishing directional charge flow between oxidation and reduction sites.

The usefulness of this approach depends on the ability to selectively assemble binuclear units inside the nanoporous silica materials. Controlled anchoring of homo-binuclear and multi-metallic sites on nanoporous materials is an important challenge that has received increasing attention by the materials chemistry and catalysis communities.[5-8] In this paper, we report two very mild synthetic methods that result in the preferential linkage of the metal precursors upon loading and anchoring inside the nanopores of MCM-41 silica material to form heterobinuclear sites. Diffuse reflectance UV-Vis, FT-IR, FT-Raman, EPR, XANES and EXAFS spectroscopy provide details of the optical and structural properties of the charge-transfer units.

2. Experimenal

2.1 Synthesis of materials

Source of chemicals: cetyltrimethyl ammonium bromide(CTABr), ammonium hydroxide (NH_4OH, 30 wt%), tetraethyl orthosilicate (TEOS), bis(cyclopentadienyl) titanium dichloride (titanocene dichloride, $TiCp_2Cl_2$), anhydrous cobalt dichloride ($CoCl_2$), ethanol (95 %), $Ti^{III}(THF)_3Cl_3$, diethylamine and hydroxylamine were obtained from Aldrich and used as received. Anhydrous acetonitrile (CH_3CN, Aldrich) was distilled over CaH_2 under N_2 atmosphere; anhydrous dichloromethane (Aldrich) was dried over 4 Å molecular sieves activated at 300 °C; triethylamine (TEA, Aldrich) was dried over sodium. $Ce(NO_3)_3$, $Cr(NO_3)_3$ and $Al(NO_3)_3$ were obtained from ACROS and used as received.

Siliceous MCM-41 was prepared as follows[9]: Template CTABr (2.2 g) was dissolved in deionized water (52 mL) containing NH_4OH (3.6 mL) at 40°C. TEOS (10 mL) was added dropwise under vigorous stirring at RT to give white gel precipitate. The gel mixture was stirred at RT for 4 hr, transferred into a Teflon lined autoclave and aged at 110 °C for 3 days. Filtration and thorough washing with deionized water gave white as-synthesized MCM-41 powder. Template removal by calcination in oxygen flow at 550 °C yielded the final product.

Grafted Ti-MCM-41 (Ti/Si = 1:100 and 3:100, respectively) was synthesized as described previously[3] using titanocene dichloride as precursor.[10,11] Ratios of metals for these and other samples indicated in this paper were determined from ICP-MS analysis of the materials.

Co^{II}-MCM-41 samples and $TiCo^{II}$-MCM-41 were also synthesized as described before[3] using the acetonitrile complex $Co^{II}(NCCH_3)_2Cl_2$ as precursor. However, in contrast to our previous procedure, no triethylamine was used during the reaction. Instead, the reaction was carried out for an additional hr at 65 °C followed by 3 hr at RT in order to enhance Co^{II} grafting. The new procedure enhances substantially the selectivity for the formation of heterobinuclear compared to isolated metal sites. Diffuse reflectance UV-Vis and FT-Raman spectra showed that no cobalt oxide clusters (Co_3O_4) and no Co hydroxide were formed after calcination at 350 °C (Figs. S1 and S2).[12]

TiCe-MCM-41 and Ce-MCM-41 sieve were synthesized as follows: 2 g of Ti-MCM-41 (or MCM-41) were placed into a Schlenk tube and dehydrated under vacuum at 250 °C for 4 hr. At the same time, $Ce(NO_3)_3$ (108 mg) was degassed in another Schlenk tube under vacuum at 80 °C and subsequently dissolved in 40 mL deaerated ethanol/water = 20/1 solution at RT. The colorless $Ce(NO_3)_3$ solution was added into the Schlenk tube containing Ti-MCM-41 (or MCM-41). The reaction mixture was stirred at RT for 1hr and at 65 °C for an additional hr. Grafting of Ce^{III} onto mesoporous silica at modestly elevated temperature using acetonitrile as solvent was recently reported by Nakamura *et al.*[4] Filtration and washing with deaerated ethanol in a glove box under N_2 atmosphere yielded the final product. Calcination at moderate temperature (350 °C) gave $TiCe^{IV}$-MCM-41 (yellow) or Ce^{IV}-MCM-41 (pale yellow).

Cr^{VI}-AlMCM-41 (Cr/Al/Si = 2:3.7:100) was synthesized using a modified version of a method reported by Klabunde.[13,14] The reason for using Al in the preparation of Cr-containing mesoporous material is two-fold: improved dispersion of Cr in the form of single sites, and stabilization of Cr centers by interaction with Al, which reduces leaching

of the metal.[15-17] Briefly, CTABr (2.04 g) was dissolved in 70 mL deionized water containing 10 mL diethylamine. TEOS (8.9 mL) was added dropwise at RT under vigorous stirring to give a white gel. The gel suspension was stirred at RT for 2 hr, followed by dropwise addition of $Al(NO_3)_3 \bullet 9H_2O$ (0.6 g) in deionized water (2 mL). The mixture was stirred at RT for an additional hr. Subsequently, $Cr(NO_3)_3$ in NH_4OH (30 wt%, 3.6 mL) was added dropwise and stirred vigorously at RT for 4 hr. The blue colored gel mixture was then transferred into a Teflon lined autoclave and aged at 110 °C for 4 days. Filtration and washing with excess deionized water resulted in blue-colored as-synthesized Cr^{III}-AlMCM-41. Calcination at 630 °C gave yellow-colored final product Cr^{VI}-AlMCM-41.

TiCr-AlMCM-41 was synthesized via redox coupling of Ti^{III} with Cr^{VI} using $Ti^{III}(THF)_3Cl_3$ precursor.[18,19] The reaction was conducted using a vacuum manifold with three Schlenk tubes. Calcined Cr^{VI}-AlMCM-41 was dehydrated in one Schlenk tube at 250 °C under vacuum for 4 hr while $Ti(THF)_3Cl_3$ was evacuated at RT for 30 min in another. Dried CH_3CN (40 mL) was deaerated by four freeze–pump-thaw cycles to remove O_2 and subsequently vacuum-distilled into the Schlenk tube containing the Ti precursor. Stirring for 10 min at RT gave a clear blue-colored acetonitrile solution of the Ti^{III} species, which was added to the Schlenk tube containing Cr^{VI}-AlMCM-41 powder under N_2 flow. The reaction mixture was stirred at RT for 1hr during which the supernatant solution became colorless. This indicated completion of the reaction by quantitative uptake of Ti^{III} into the Cr-AlMCM-41 material. Filtration and washing with excess deaerated CH_3CN solution gave blue-colored TiCr-AlMCM-41 product (termed as-synthesized material). Calcination at moderate temperature of 350 °C yielded bright

blue TiCr-AlMCM-41. FT-IR and FT-Raman spectra did not show any trace of THF or solvent, confirming that the resulting material is free of organics.

2.2 Spectroscopic characterization

Optical spectra were measured on a Shimadzu model UV-2100 spectrometer equipped with an integrating sphere model ISR260. For measurement of mesoporous silica samples, the powder was pressed into a self-sustaining pellet and mounted in a home-built vacuum cell for diffuse reflectance measurements. Barium sulfate was used as reference. Fourier-transform Infrared (FT-IR) spectra were recorded on a Bruker model IFS66V spectrometer equipped with liquid N_2 cooled MCT detectors Kolmar model KMPV8-1-J2 (8 μ bandgap), Infrared Associates (25 μ bandgap), or a DTGS detector (for 600–400 cm^{-1} region). Pressed self-sustaining pellets of nanoporous silica powder (5 mg) were mounted in a transmission infrared vacuum cell equipped with KBr windows. The loading of the infrared cell was done under N_2 atmosphere. All FT-IR spectra were recorded after evacuation of the sample cell at RT for at least 1 hr. FT-Raman spectra were recorded with a Bruker model FRA-106 spectrometer equipped with a Nd:YAG laser source emitting at 1.064 μm (9394.3 cm^{-1}, 525 mW) and a liquid N_2 cooled Ge detector. Samples for the FT-Raman measurement were prepared by pressing the powder on an aluminum sample holder, or by loading the powder into a quartz tube in a N_2 glove box in the case of air-sensitive materials.

Powder X-ray diffraction (XRD) measurements were performed on a Siemens model D500 diffractometer equipped with Ni-filtered Cu K_α radiation source (k = 1.5406 Å). Typically, an accelerating voltage of 40 kV and a current of 30 mA were used. The textural uniformity of the MCM-41 materials was recorded for the 2θ range from 1.5° to

8° with a step size of 0.02° (d-spacing approx. 40 Å[20], Fig S3 of supporting information).[12]

X-band electron paramagnetic resonance (EPR) spectra of Cr^{V} and Cr^{III} were recorded on a Varian E-109 spectrometer equipped with an E-102 microwave bridge (microwave frequency 9.25 GHz). The temperature of the sample was maintained at 20 K during the measurements using an Air Products Helitran liquid helium cryostat. In order to facilitate comparison, the same instrument parameters were used for the recording of EPR spectra of all samples: modulation amplitude of 3.2 G for Cr^{V} and 32 G for Cr^{III}, scanning field range of 400 G for Cr^{V} and 4000 G for Cr^{III}, modulation frequency of 100 KHz, microwave power of 1 mW, receiver gain of 3.2×10^{3}, center field at 3340 G, scanning rate of 2 min/scan, and time constant of 0.25 s. EPR spectra of Co^{II} were recorded with the same experimental parameters as Cr^{III} except that the center field was set to 2700 G with sweep width of 3200 G. Samples were weighed accurately (range 12-15 mg) prior to loading into the EPR tubes, and the relative intensity of the EPR spectra were normalized accordingly. Uncertainties of g values derived form the measurements are $\pm$ 0.002.

Extended X-Ray Absorption Fine Structure (EXAFS) spectra were recorded at Beamline 7-3 at SSRL (Stanford Synchrotron Radiation Laboratory). The synchrotron ring SPEAR was operated at 3.0 GeV with a beam current in the range of 100–500 mA. The incident beam intensity was monitored using a passivated implanted planar silicon (PIPS) detector installed in a N_2-filled ion chamber (I_0) positioned in front of the sample. An incident X-ray beam with a spot size of 2×15 mm^2 and a flux of $\sim 2 \times 10^{12}$ photons/sec @ 100 mA/9000 eV with 1×4 mm^2 aperture was used for the EXAFS

experiments. The sample was evenly placed on the sample holder with a dimension of 2.5 × 10 mm^2 and covered with metal free transparent tape. Energy resolution ($\Delta E/E = 1 \times 10^{-4}$) of the unfocused incoming X-rays with energy range of 4600-37000 eV was achieved using a Si(220) double-crystal monochromator, which was detuned to 50 % of maximal flux to attenuate harmonic X-rays. The samples were placed at an angle of 45° relative to the X-ray beam and kept at a constant temperature of 10 ± 1 K at ambient pressure using an Oxford CF-1208 continuous-flow liquid He cryostat. The X-ray absorption spectra were acquired by XAS-Collect software in fluorescence mode using a 30-element Ge detector array, and were referenced against I_0. The energy reference spectra were collected concurrently with sample data by placing a standard sample (Cr foil (K-edge 5989.0 eV), Co foil (K-edge 7709 eV), CeO_2 (L_3 edge 5723 eV)) between two N_2-filled ion chambers which were positioned behind the sample.

Data processing and analysis were carried out using Ifeffit version 1.2.10 EXAFS analysis software package (integrated with SixPack, Athena, Artemis, Feff 6.02, Hephaestus, autobk).[21] Preliminary data processing was performed using SixPack. Energy calibration, final data averaging by aligning and merging all scans, background subtraction (including pre-edge subtraction and spline correction), as well as forward Fourier Transform (FT) of κ^3 weighted data (at Kaiser Bessel window) were performed using Athena. The first inflection points in the first derivative of Ce L_3-edge, Co and Cr K-edge spectra were used for energy calibration. The threshold energies (E_0) at which κ = 0 were set at 5995 eV for Cr and 7715 eV for Co. To show the real distances of the first shell Co-O and Cr-O, the κ^3-weighted FT-EXAFS spectra reported in this paper were phase-corrected using O as the backscatterer.

3. Results and Discussion

3.1 Selective assembly of hetero-binuclear MMCT units on silica nanopore surface

The selective assembly of heterobinuclear units on the surface of silica nanopores through sequential precursor loading requires a mild synthetic approach that takes advantage of specific chemical interactions between the partner metals. In this section, we will present the results of two different methods, both leading to the preferential formation of oxo-bridged heterobinuclear units at the expense of isolated metal centers. One method exploits the higher acidity and, hence, higher reactivity of titanol compared to surface silanol OH groups. The second method takes advantage of the selective redox reactivity of metal precursors towards already anchored metal centers.

3.1.1 Selectivity based on acidity difference between TiOH and SiOH

When monitoring the uptake of the donor metal precursor $Co^{II}(NCCH_3)_2Cl_2$ into MCM-41 or Ti-MCM-41 particles from acetonitrile solution by UV-Vis spectroscopy of the supernatant over a 2 hr period, more than an order of magnitude faster rate was observed for the silica sieve that contains tripodally anchored $(OSi)_3TiOH$ groups on the pore surface. As shown in Table 1, the uptake of Co^{II} onto Ti-MCM-41 containing 1 percent Ti exceeds the value for plain MCM-41 by a factor of 12. According to ICP analysis of the resulting TiCo-MCM-41 material, the Ti/Co ratio is 12, and the increase of the Co content compared to monometallic Co-MCM-41 is over a factor of 50. Similarly, the uptake of Ce^{III} ions dissolved in ethanol increased from 9 percent in the

case of MCM-41 to 20 percent for Ti-MCM-41(1%). IPC analysis of the bimetallic TiCe-MCM-41 material gave a factor of 6.5 increase of the Ce loading compared to plain MCM-41, and a Ti/Ce ratio of 7 (Table 1; note that differences in the data on precursor uptake by supernatant measurement on the one hand and ICP analysis of the solid material on the other reflect the removal of unanchored metal centers upon washing of the synthesized material).

Comparison of the OH infrared absorption bands of free (non-H bonded) SiOH groups after calcination of the resulting materials at moderate temperature (350 ^{o}C) confirms these trends. In the case of Ce^{III} grafting onto pure mesoporous silica, the intensity of the band of free SiOH in the range 3743-3745 cm^{-1} of MCM-41[22,23] decreased by only 10 percent (Fig. 1B) while the intensity loss was 30 percent in the case of Ti-MCM-41 (Fig. 1A). We attribute the more pronounced loss of free SiOH upon grafting of Ce precursor onto Ti-MCM-41 to the formation of more Ce-O-Si bonds as one would expect from the increased loading of Ce^{III}. Similar observations by FT-IR were made in the case of Co^{II} grafting.

The much larger uptake of Ce^{III} and Co^{II} into Ti-MCM-41 is attributed to the higher acidity, hence higher reactivity of TiOH groups with metal precursors compared to SiOH groups.[24] The acidity difference is manifested in the lower OH stretch frequency of TiOH (3676 cm^{-1})[25,26] compared to the SiOH group at 3745 cm^{-1}. These results show that one can exploit OH group acidity as a general synthetic method for the selective assembly of oxo-bridged heterobinuclear units on silica nanopore surfaces, which requires avoidance of strong base for the grafting procedure.

3.1.2 Selectivity through redox coupling

The preferential formation of heterobinuclear units compared to isolated metal centers on silica nanopore surfaces can in principle be achieved by exploiting selective redox reactivity of one metal with another.[18,19] To this end, we have explored the assembly of TiOCr units in MCM-41 by first preparing a material that contains tetrahedral Cr^{VI} centers anchored on the nanopore surface. The synthesis and characterization of Cr^{VI}-AlMCM-41 by optical, FT-Raman and FT-IR spectroscopy has been reported previously,[27] and new structural details derived from X-ray absorption measurements are presented in Sect. 3.3.2 below. Exposure of the material to a solution of $Ti^{III}(THF)_3Cl_3$ in acetonitrile resulted in essentially quantitative reaction of the precursor within 1 h at RT, while only 3 percent could be loaded into plain AlMCM-41 under the same experimental conditions. According to ICP analysis, an equimolar amount of Ti was incorporated into Cr-AlMCM-41. No Ti could be detected by ICP in Ti-only AlMCM-41 using this precursor, which implies that the increase of the Ti content in the TiCr-AlMCM-41 material is at least a factor of 150 based on the ICP detection limit. This effect of Cr can readily be explained by the redox reaction of Cr^{VI}=O with the Ti^{III} complex

$$Cr^{VI}=O + Ti^{III} \rightarrow Cr^{V}\text{-}O\text{-}Ti^{IV} \qquad (1)$$

The accompanying change of the yellow color of Cr^{VI}-AlMCM-41 to pale blue indicates that a substantial fraction of the Cr centers undergo reduction to Cr^{III}. Such redox interaction cannot occur with the non-reducible Si centers, which explains the selectivity.

It is well established that Cr^{VI} centers of calcined Cr-AlMCM-41 have distorted tetrahedral coordination and occur predominantly as $(SiO)_2Cr(=O)_2$ sites at the nanopore

surface.[15,16,28] A characteristic spectroscopic signature of this site is a sharp band in the FT-Raman spectrum of dehydrated Cr^{VI}-AlMCM-41 at 987 cm^{-1} assigned to the symmetric O=Cr^{VI}=O stretch (Fig. 2A, trace (a)).[27,29] More accurately, one of the linkages may involve an Al center that partially compensates for the large positive charge of Cr^{VI}.

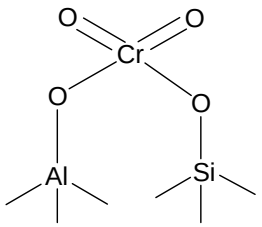

Isolated T_d Cr^{VI}

Redox coupling of the Cr^{VI} centers with Ti^{III} was confirmed by diffuse reflectance (DRS) UV-Vis spectroscopy as well as FTIR, FT-Raman and EPR (X-band) spectroscopy. As can be seen from Fig. 3, trace (a), only a weak absorption with a maximum around 280 nm and a very weak band at 568 nm are observed when plain AlMCM-41 is exposed to Ti^{III} precursor, indicating loading of only trace amounts of Ti^{III}. The latter band is a characteristic of d-d absorption of Ti^{III}, shown in the inset of Figure 3.[30] By contrast, comparison of the spectra of calcined Cr^{VI}-AlMCM-41 before and after exposure to Ti^{III}, trace (b) and (c) of Fig. 3, reveals substantial loading and interaction with Ti. The 263, 357, and 457 nm peaks of the O^{II}-Cr^{VI} $\rightarrow$ O^{I}-Cr^{V} ligand to metal charge transfer (LMCT) band[15] of Cr^{VI}-AlMCM-41 decrease precipitously upon reaction with Ti^{III} precursor indicating reduction of most Cr^{VI} centers. Concurrent growth of a broad band with a maximum at 654 nm, Fig. 3 trace (c), indicates the formation of Cr^{III} and/or Cr^{V}.[15,31]

FT-Raman spectra show a complete loss of the symmetric O=Cr^{VI}=O stretch upon reaction with $Ti^{III}(THF)_3Cl_3$. This is seen by the disappearance of the $\nu_s(CrO_2)$ absorption of dehydrated (987 cm^{-1}, Fig. 2A trace (a)) or dehydrated Cr^{VI}-AlMCM-41 (901 cm^{-1}, trace (b))[15,32]; the band is completely vanished upon exposure to Ti^{III} precursor (as-synthesized TiCr-AlMCM-41 sample, Fig. 2A trace (c); after calcination at 350 ^oC, Fig. 2A trace (d)). At the same time, anchoring of Ti is signaled by growth in the resulting TiCr-AlMCM-41 spectrum at 925 cm^{-1} characteristic for Si-O stretch modes perturbed by a metal center.[33,34] Likewise, Fig. 2B shows that the asymmetric O=Cr^{VI}=O stretch in the FT-IR spectrum disappears upon Ti^{III} loading (910 cm^{-1}, dehydrated sample, trace (a); 893 cm^{-1}, hydrated sample, trace (b)).[11] The resulting TiCr-AlMCM-41 spectra, shown in Fig. 2B trace (c) (as-synthesized material) and trace (d) (after calcination at 350 ^oC) exhibit a broad shoulder at 930 cm^{-1} which is due to Si-O stretch modes perturbed by the presence of Ti centers.[1,22] Hence, Raman and FT-IR spectra strongly support our interpretation that the reaction of Cr^{VI}=O groups with Ti^{III} leads to the reduction of Cr centers and anchoring of Ti. No FT-Raman bands characteristic of di- or polychromate (1000-1100 cm^{-1})[15,27] were detected in the final TiCr-AlMCM-41 material. Furthermore, the formation of Ti oxide or Cr_2O_3 clusters was excluded based on FT-Raman measurements (Fig. S4).[12]

EPR spectra recorded upon Ti^{III} grafting allowed us to directly monitor the formation of Cr^V (Fig. 4A) and Cr^{III} species (Fig. 4B). While trace amounts of Cr^V are detected in the calcined Cr^{VI}-AlMCM-41 material (Fig. 4A, spectrum (a)), a large increase of the signal occurs upon Ti^{III} treatment due to reduction of Cr^{VI} to Cr^V (Fig. 4A, spectrum (b)). At the same time, spectrum (b) of Fig. 4B shows a marked growth of the

EPR signal of Cr^{III} centers confirming that a substantial fraction of the Cr sites undergo multi-electron reduction to Cr^{III}, the most stable reduced form of Cr on silica supports.[15] Closer inspection of the EPR spectra reveals more than one type of residual Cr^{V} signal present in the calcined Cr^{VI}-AlMCM-41 material (Fig. 4A, spectrum (a)). Observed Cr^{V} γ EPR signals are: a square-pyramidal (S_p) Cr^{V} with $g_{\perp} = 1.977$ and $g_{//} = 1.964$, and a distorted tetrahedral (T_d) Cr^{V} with $g_{\perp} = 1.975$ and $g_{//} = 1.890$.[15,35] In addition, a very weak broad, 600 G wide β EPR signal of octahedral (O_h) Cr^{III} with $g_{iso} = \sim 2.029$ is observed (Fig. 4B, spectrum (a)).[15,35,36] Interestingly, the g values of the Cr^{V} signal that grows upon reaction of Cr^{VI}=O with Ti^{III}, $g_{\perp} = 1.988$ and $g_{//} = 1.960$ (Fig. 4A, spectrum (b)) indicate that a new Cr^{V} site is generated, possibly because of the link that is formed to Ti. Note that upon calcination the Cr^{III} EPR signal partially decreases while the Cr^{V} signal broadens, indicating partial oxidation of Cr^{III} to Cr^{V} (Fig. 4, spectrum (c)).

We conclude that monitoring of $Ti^{III}(THF)_3$ exposure to Cr^{VI}-AlMCM-41 sieve by optical, vibrational and EPR spectroscopy demonstrates redox reaction that results in selective grafting of Ti onto Cr centers.

3.2. Optical and EPR spectroscopic properties of MMCT units

The heterobinuclear units assembled on the surface of nanoporous silica, with one metal (Ti^{IV}) acting as electron acceptor and the other as electron donor (Co^{II}, $Ce^{III,}$ Cr^{III}) possess visible light absorption properties originating from a MMCT transition. In this section, characterization of the units by optical and EPR spectroscopy will be presented and discussed.

For the TiCo system, Co may possess either high spin or low spin state electronic configuration. Low spin Co usually occurs in O_h coordination, while high spin Co could be either O_h or T_d (Fig. S5).[12,38-40] To address this question, we have recorded EPR spectra of Co^{II}-MCM-41 and $TiCo^{II}$-MCM-41 shown in Fig. 5 trace (a) and (b), respectively. The large signal with $g_\perp = 5.107$ (Co^{II}-MCM-41) and $g_\perp = 5.250$ ($TiCo^{II}$-MCM-41) and the accompanying small $g_{//} = 2.032$ (2.034) signal clearly demonstrate that the grafted Co^{II} center, whether isolated or linked to Ti is high spin Co^{II}.[40-42] The result is consistent with the diffuse reflectance UV-Vis spectra of Co-MCM-41 and $TiCo^{II}$-MCM-41, shown in Fig. 6. The three d-d absorption bands with maxima at 535, 593 and 650 nm signal tetrahedral coordination (Co^{II} $^4A_2(F) \rightarrow {}^4T_1(P)$ transition is split into triplets by spin-orbit coupling).[3,39] Note that the absorption energy of the three d-d Co^{II} spin-orbit components remains essentially unchanged upon assembly of hetero-binuclear $TiOCo^{II}$ units. We conclude from the EPR and optical data that the grafted Co^{II} centers are mainly high spin and in tetrahedral coordination. The $TiCo^{II}$-MCM-41 material shows an additional absorption extending from UV into the deep red spectral region (~650 nm), not present in the Co only material. The new absorption, highlighted in Fig. 6 as shaded area, is attributed to the $Co^{II} + Ti^{IV} \rightarrow Co^{III} + Ti^{III}$ MMCT transition.[3] While formation of Co_3O_4 clusters would give a similar additional absorption, this possibility was ruled out by FT-Raman spectroscopy (Supporting Information Fig. S1, spectra (b) and (c)).[12,43] TiCo MMCT transition has been encountered previously in Co doped titanate.[44]

Fig. 7 shows the diffuse reflectance UV-Vis spectra of (a) Ce^{III}-MCM-41 (amplified by 6.5, see figure caption); (b) sum of Ti-MCM-41 and (a); (c) $TiCe^{III}$-MCM-41. Ce^{III}-MCM-41 exhibits a weak 4f → 5d absorption with a maximum at 268 nm and

an onset at 350 nm.[45,46] The Ti-MCM-41 sieve features the $O^{II} \rightarrow Ti^{IV}$ LMCT band at ca. 220 nm with an absorption onset around 340 nm.[1] On the other hand, the bimetallic $TiCe^{III}$-MCM-41 sieve has a continuous absorption in the visible region extending to 525 nm that is absent in the mononuclear materials. It is assigned to the MMCT transition $Ce^{III} + Ti^{IV} \rightarrow Ce^{IV} + Ti^{III}$,[44,46,47] first reported as binuclear unit in mesoporous silica by Nakamura *et al.*[4] Metal-to-metal charge-transfer is the only transition we can conceive of for a low energy absorption formed upon interaction of a Ti^{IV} and Ce^{III} center. Furthermore, the isopropanol + O_2 photoreaction observed upon excitation of the transition is consistent with the MMCT nature of the absorption.[4] The possibility of CeO_2 clusters contributing to this new absorption of the bimetallic material was ruled out by the absence of a characteristic CeO_2 band at 465 cm^{-1} in FT-Raman spectrum (Fig S6).[12,47] Upon oxidation of Ce^{III} to Ce^{IV} by calcination of TiCe-MCM-41 at 350 ^oC, the DRS at visible wavelengths looks the same as the calcined monometallic Ce^{IV}-MCM-41 spectrum (Fig. S7)[12] and originates from the Ce^{IV} LMCT (O^{II}-Ce^{IV}) transition.[48,49] Disappearance upon oxidation of the new absorption observed for the $TiCe^{III}$ units supports the assignment to a MMCT transition between Ce^{III} and Ti^{IV}.

As discussed above (Sect. 3.1.2), as-prepared TiCr-AlMCM-41 features Cr in oxidation state III and V, while calcined Cr-AlMCM-41 has Cr mostly in oxidation state VI. Cr centers in oxidation state V and VI are highly oxidizing and unlikely to give rise to a visible MMCT absorption when linked to Ti.[37] To obtain a visible light-absorbing TiCr charge-transfer system, Cr centers were reduced to Cr^{III} using aqueous hydroxylamine. Diffuse reflectance UV-Vis spectra of the resulting reduced $TiCr^{III}$-AlMCM-41 and Cr^{III}-AlMCM-41 are shown in Fig. 8. The two bands of Cr^{III}-AlMCM-41 with maxima at 430

and 600 nm (Fig. 8, trace (a)) originate from d-d transition of octahedrally coordinated Cr^{III} (spin-orbit components $^4A_{2g} \rightarrow {}^4T_{2g}$ and $^4A_{2g} \rightarrow {}^4T_{1g}$, respectively)[15,31], while the intense absorption below 380 nm is due to LMCT of O^{II}-Cr^{III}.[31] No LMCT bands due to Cr^{VI} are observed in the diffuse reflectance spectrum indicating that Cr^{VI} is completely reduced to Cr^{III}. The bimetallic $TiCr^{III}$-AlMCM-41 sieve, Fig. 8 trace (c), shows absorption at wavelengths longer than 340 nm that is not present in the sum of the spectra of Cr^{III}-AlMCM-41 + Ti-AlMCM-41 (Fig. 8, spectrum (b)). The additional intensity above 600 nm might be caused by a small shift of the $^4A_{2g} - {}^4T_{1g}$ component of the Cr^{III} (d-d) transition due to coupling with the Ti center. However, it is very unlikely that the new absorption of the $TiOCr^{III}$ moiety between 600 and 340 nm merely reflects a change of the Cr^{III} ligand field spectrum because of linkage to Ti. We conclude that $TiOCr^{III}$ units feature a $Ti^{IV} + Cr^{III} \rightarrow Ti^{III} + Cr^{IV}$ MMCT absorption extending from about 330 nm into the red spectral region. Assignment to a MMCT transition is supported by the direct observation of Ti^{3+} by EPR spectroscopy if the $TiOCr^{III}$ unit is coupled to an Ir oxide nanocluster that acts as electron donor; in this case, back electron transfer is blocked by the reduction of transient Cr^{IV} by the electron donor.[50] Mixed TiCr oxide minerals are again precedents for this type of charge transfer absorption.[51,52]

3.3. XANES and preliminary EXAFS characterization of binuclear units

X ray absorption spectroscopy is an essential tool for investigating the molecular structure of non-crystalline materials at the atomic level. In this work, XANES measurements for all three binuclear systems and EXAFS of TiOCr sites are used to explore in more detail the structural properties of the assembled hetero-binuclear units

and to corroborate the formation of covalently linked binuclear groups on the surface of nanoporous silica.

3.3.1 TiOCo units

Co K-edge spectra of Co^{II}-MCM-41 and $TiCo^{II}$-MCM-41 are shown in Fig. 9A, with the small pre-edge bands displayed on an expanded scale in Fig. 9B. The pre-edge peaks at 7709.7 eV for Co^{II}-MCM41 and 7709.9 eV for $TiCo^{II}$-MCM41 are due to partially allowed, dipole forbidden 1s $\rightarrow$ 3d transition of T_d coordinated Co^{II} [53] in agreement with the result from diffuse reflectance UV-Vis spectra discussed above. Compared to solely Co containing Co^{II}-MCM-41, binuclear $TiCo^{II}$-MCM-41 material shows a shift of the peak by 0.2 eV toward higher energy accompanied by an intensity decrease. We have previously reported the same effect of $TiCo^{II}$ binuclear unit formation on the pre-edge 1s $\rightarrow$ 3d peak of the Ti edge.[3] The shift is caused by a distortion of the metal center from tetrahedral geometry as it is expected to occur upon formation of an oxo-bridge to a metal partner. We conclude that the XANES spectra exhibit behavior consistent with the formation of a covalent MMCT unit.

3.3.2 TiOCr units

Cr K-edge XANES spectra of Cr-AlMCM-41 and TiCr-AlMCM-41 with the Cr center in various oxidation states are shown in Fig. 10A, with the corresponding detailed pre-edge peaks presented in Fig. 10B. Both the pre-edge absorption and the position of the K-edge furnish important information on coordination geometry and oxidation state of the metal. The XANES spectrum of calcined Cr^{VI}-AlMCM-41 (spectrum (a) of Fig.

10A) shows a characteristic sharp intense pre-edge peak at 5993.4 eV due to the partially allowed dipole forbidden 1s-3d transition of T_d coordinated Cr^{VI} [15,28,53] (in Fig. 10B spectrum (a), the observed signal was divided by 10 to facilitate comparison with other spectra shown in the panel). The peak intensity of this pre-edge band relative to the height of the plateau between K-edge[54] and the onset of the EXAFS region is close to one, which implies that essentially all Cr centers are in tetrahedral Cr^{VI} configuration.[29] Furthermore, since the position of the Cr-AlMCM-41 K-edge relative to that of metallic Cr is linearly dependent on the oxidation state of the metal,[55] the oxidation state can also be derived from the K-edge energy. The K-edge of the metallic Cr reference was observed at 5990 eV (first derivative peak) while that of Fig. 10A spectrum (a) lies at 6008.4 eV. Hence, the shift is 18.4 eV, which is typical for Cr^{VI}.[53] After redox coupling of Cr^{VI} with Ti^{III} precursor, spectrum (b) of Fig. 10A is observed with the K-edge located at 6000.6 eV, corresponding to $\Delta E = 10.6$ eV. The shift implies that the Cr centers of as-synthesized TiCr-AlMCM-41 are mainly Cr^{III}.[53] Nevertheless, some centers remain as S_p-coordinated Cr^{V} based on our EPR measurements (Fig. 4A). Concurrently, the large pre-edge band of Cr^{VI} is replaced by a much less intense doublet at 5990.6 and 5993.4 eV (Fig. 10A spectrum (b)) characteristic of the 1s-3d absorption of octahedral Cr^{III}.[56] Subsequent mild calcination of TiCr-AlMCM-41 at 350 ^{o}C (Fig. 10A, spectrum (c)) results in a small blue shift of the K-edge to 6001 eV indicating partial oxidation of Cr^{III} to higher oxidation states. Corresponding EPR spectra (Fig. 4) confirm that mainly T_d and S_p coordinated Cr^{V} is produced. The extent of oxidation is very small as manifested by the small K-edge shift and only minor intensity changes of the Cr^{III} pre-edge peaks at 5990.6 and 5993.4 eV (Fig. 10B, spectrum (c)).

These X-ray absorption spectra reveal that our method of preparing $TiCr^{III}$ units by reduction with hydroxylamine is quantitative. In the XANES spectrum of hydroxylamine-reduced TiCr-AlMCM-41 (Fig. 10A, spectrum (d)), doublet pre-edge peaks due to octahedrally coordinated Cr^{III} are observed at 5990.6 eV and 5993.4 eV. Comparison with literature results shows that the there is no contribution of Cr^{VI} to the 5993.4 eV absorption.[53] Furthermore, no Cr^{V} is present according to EPR spectroscopy. The K-edge shift ΔE is 10.6 eV as expected for a Cr^{III} sample.

The Fourier-transformed EXAFS function of the Cr K-edge of Cr^{VI}-AlMCM-41 (χ^3 weighted and phase corrected with O as backscatterer, Fig. 11A spectrum (a)) shows a single peak at a distance of 1.58 Å assigned to backscattering from the first shell of O atoms. The short bond is consistent with the metal in its highest Cr^{VI} oxidation state.[28] Preliminary EXAFS curve fitting shows that two Cr=O distances of 1.59 A and two Cr-O bond distances of 1.89 A are involved in this first shell peak, in agreement with the expected geometry for tetrahedral Cr^{VI}. The absence of any additional peak indicates that Cr^{VI} centers are well dispersed and no clusters are formed. By contrast, the FT-EXAFS result of the as-synthesized TiCr-AlMCM-41 material, Fig. 11A trace (b) gives two peaks: A first shell signal at 2.02 Å corresponding to the Cr-O distance and a second shell peak at 2.70 Å (apparent distance). The considerably longer Cr-O bond is in agreement with the oxidation state change of Cr from +6 to +3.[28,57] Since we can rule out the presence of Cr oxide clusters based on our FT-Raman measurements, the new peak at 2.7 Å is assigned to backscattering from Ti^{IV} centers. This distance is close to another case of an oxo-bridged heterobinuclear unit in mesoporous silica we are aware of, namely 2.8 A for Ti-O-Ge on MCM-41 (Ti-O-Ge bond angle of 106°).[58] Observation of a Ti···Cr distance

convincingly demonstrates the formation of a hetero-binuclear Ti-O-Cr unit on the silica nanopore surface. After calcination at 350 °C (Fig. 11A, spectrum (c)), the Cr-O distance again shortens, but only slightly, to 1.97 Å. This corroborates the observation of only minor changes in the XANES spectra and K-edge position discussed in the preceding paragraph, indicating that only a small fraction of Cr^{III} centers are oxidized by the process. At the same time, the Ti···Cr distance is shortened as well, to 2.58 Å (apparent distance), an expected consequence of the shortened Cr-O bond.

The interpretation of these EXAFS results is further supported by examination of the Cr K-edge EXAFS FT spectra of samples treated by hydroxylamine, shown in Fig. 11, panel B. Comparison of spectra (a) and (b) confirms that reduction of Cr^{VI}-AlMCM-41 by hydroxylamine causes a lengthening of the Cr-O distance from 1.58 Å to 2.00 Å, which is the same effect within experimental error as observed upon preparation of TiCr-AlMCM-41 by treatment with Ti^{III} precursor. Furthermore, reduction of calcined TiCr-AlMCM-41 using hydroxylamine results in a shift of both first and second shell peaks toward longer distances, i.e., from 1.97 Å to 2.07 Å for the first peak and from 2.58 Å to 2.7 Å (apparent distance) for the second peak, indicating complete reduction of chromium centers to Cr^{III}. Restoration of the second shell peak to the distance of 2.7 Å, which is the same distance observed for the as-synthesized TiCr-AlMCM-41, manifests the integrity of the binuclear Ti-O-Cr unit under redox treatment.

3.3.3 TiOCe units

Absorption spectra of the L_3-edge of Ce are very useful for probing the Ce oxidation state because of the characteristic bands for +3 and +4 state. Ce^{III} has a single

peak at 5727.0 (5728.0) eV originating from the 2p → 5d transition. Ce^{IV} exhibits a doublet with maxima at 5729.0 eV (assigned to the transition from 2p to admixed [5d + 4f] state) and 5737.0 eV (2p → 5d transition).[59,60] Hence, the spectra afford a straightforward way of assessing the oxidation state of grafted Ce in the nanoporous material as previously demonstrated.[4] For Ce^{III}-MCM-41 and $TiCe^{III}$-MCM-41 samples, the L_3-edge spectrum, shown in Fig. 12A, is dominate by the Ce^{III} edge peak at 5727 (5728) eV. The weak shoulder at 5738 eV might be due to traces of Ce^{IV} (the lower energy band of the doublet at 5729 eV would be overlapped by the intense Ce^{III} absorption), probably introduced as an impurity of the precursor $Ce(NO_3)_3$ sample. We conclude that in the as-synthesized materials, Ce is mainly grafted as Ce^{III}. After calcination at a moderate temperature of 350 °C, a doublet with peaks at 5729.0 eV and 5737.0 eV was observed, with no evidence for residual Ce^{III} (Fig. 12B). The very weak shoulder at 5720 eV in both calcined monometallic Ce^{IV} and bimetallic $TeCe^{IV}$ samples is due to dipole-forbidden 2p → 4f transition, which is a consequence of 5d admixtures to the 4f state in Ce^{IV}.[60] The definitive assignment of Ce oxidation state based on the L_3-edge absorption measurements add strong support for our interpretation of the optical spectra of Ce-MCM-41 and TiCe-MCM-41 materials presented in Fig. 7.

4. Conclusions

Controlled assembly and anchoring of oxo-bridged heterobinuclear units on the inner surface of mesoporous silica has been demonstrated. By exploiting acidity

differences of surface OH groups while avoiding the customary use of strong base, or by taking advantage of the specific redox reactivity of one metal precursor towards another, we have accomplished highly selective attachment of the second metal precursor to the initially anchored metal center to form $TiOCr^{III}$, $TiOCo^{II}$ and $TiOCe^{III}$ sites on the pore surface of MCM-41 silica sieve. X-ray absorption spectroscopy combined with results from EPR, FT-infrared and FT-Raman spectroscopy furnish proof for the formation of covalently linked binuclear units and reveal details about oxidation state and the oxide coordination environment of donor and acceptor centers. For the TiCr material, preliminary analysis of Cr K-edge EXAFS data reveals a Ti center in the second coordination sphere at a distance expected for an oxo-bridged unit. Moreover, the EXAFS data confirm the integrity of the unit under repeated oxidation/reduction treatment of the Cr center. Curve fitting analysis of EXAFS data of the three binuclear materials, all of which exhibit second shell interactions, is in progress. The objective is to attain detailed structural knowledge of these oxo-bridged units on solid supports approaching that of homogeneous organometallic metal-to-metal charge-transfer systems such as cyano bridged complexes.[61-64]

The three heterobinuclear sites presented here possess metal-to-metal charge-transfer absorptions that extend deep into the visible spectral region. The flexibility of assembling units with desired donor or acceptor metal and oxidation state is crucial for developing charge-transfer pumps with selectable redox potentials and tunable optical absorption properties. Matching of the redox potentials of donor and acceptor centers of the charge-transfer chromophores to those of multi-electron transfer catalysts is the key for developing photocatalytic units that are thermodynamically efficient. The ability to

assemble units with selected redox energetics is equally critical for accomplishing efficient directional electron transport between photocatalytic oxidation and reduction sites. The mild synthetic methods presented here open up opportunities for developing robust photocatalytic sites on nanostructured supports for demanding photosynthetic applications.

Acknowledgements

This work was supported by the Director, Office of Science, Office of Basic Energy Sciences, Division of Chemical, Geological and Biosciences of the U.S. Department of Energy under Contract No. DE-AC02-05CH11231. The authors thank Dr. Yulia Pushkar and the group of Dr. Vittal Yachandra at LBNL for use of their EPR facility, and for assistance in XAFS data collection and analysis. Portions of this research were carried out at the Stanford Synchrotron Radiation Laboratory, a national user facility operated by Stanford University on behalf of the U.S. Department of Energy, Office of Basic Energy Sciences. The SSRL Structural Molecular Biology Program is supported by the Department of Energy, Office of Biological and Environmental Research, and by the National Institutes of Health, National Center for Research Resources, Biomedical Technology Program.

References

1. Lin, W.; Frei, H. *J. Phys. Chem. B* **2005**, *109*, 4929-4935.
2. Lin, W.; Frei, H. *J. Am. Chem. Soc.* **2005**, *127*, 1610-1611.
3. Han, H.; Frei, H. *Microporous Mesoporous Mater.* **2007**, *103*, 265-272.
4. Nakamura, R.; Okamoto, A.; Osawa, H.; Irie, H.; Hashimoto, K. *J. Am. Chem. Soc.* **2007**, *129*, 9596.
5. Holland, A.W.; Li, G.; Shahin, A.M.; Long, G.J.; Bell, A.T.; Tilley, T.D. *J. Catal.* **2005**, *235*, 150-163.
6. Pillinger, M.; Goncalves, I.S; Lopes, A.D.; Ferreira, P.; Rocha, J.; Zhang, G.; Schafer, M.; Nuyken, O.; Kuhn, F.E. *Phys. Chem. Chem. Phys.* **2002**, *4*, 696-702.
7. Taha, Z.A.; Deguns, E.W.; Chattopadhyay, S.; Scott, S.L. *Organometallics* **2006**, *25*, 1891-1899.
8. Thomas, J.M.; Raja, R.; Lewis, D.W. *Angew. Chem. Int. Ed.* **2005**, *44*, 6456-6482.
9. Lin, W.; Han, H.; Frei, H. *J. Phys. Chem. B* **2004**, *108*, 18269-18273.
10. Marchese, L.; Maschmeyer, T.; Gianotti, E.; Coluccia, S.; Thomas, J.M. *J. Phys. Chem. B* **1997**, *101*, 8836.
11. Maschmeyer, T.; Rey, F.; Sankar, G.; Thomas, J.M. *Nature* **1995**, *378*, 159.
12. Supporting Information
13. Rodrigues, S.; Ranjit, K.T.; Uma, S.; Martyanov, I.N.; Klabunde, K.J. J. Catal. **2005**, *230*, 158-165.
14. Rodrigues, S.; Uma, S.; Martyanov, I.N.; Klabunde, K.J. *J. Photochem. Photobiol. A* **2004**, *165*, 51-58.

15. Weckhuysen, B.M.; Wachs, I.E.; Schoonheydt, R.A. *Chem. Rev.* **1996**, *96*, 3327-3349.

16. Weckhuysen, B.M.; Ridder, L.M.D.; Grobet, R.J.; Schoonheydt, R.A. *J. Phys. Chem.* **1995**, *99*, 320-326.

17. Weckhuysen, B.M.; Verberckmoes, A.A.; Buttiens, A.L.; Schoonheydt, R.A. *J. Phys. Chem.* **1994**, *98*, 579-584.

18. Pilato, R.S.; Rubin, D.; Geoffrey, G.L.; Rheingold, A.L. *Inorg. Chem.* **1990**, *29*, 1986-1990.

19. Liston, D.J.; Kennedy, B.J.; Murray, K.S.; West, B.O. *Inorg. Chem.* **1985**, *24*, 1561-1567.

20. Beck, J.S.; Vartuli, J.C.; Roth, W.J.; Leonowicz, M.E.; Kresge, C.T.; Schmitt, K.D.; Chu, C.T.W.; Olson, D.H.; Sheppard, E.W.; McCullen, S.B.; Higgins, J.B.; Schlenker, J.L. *J. Am. Chem. Soc.* **1992**, *114*, 10834-10843.

21. Ravel, B.; Newville, M. *J. Synchrotron Rad.* **2005**, *12*, 537-541.

22. Marchese, L.; Gianotti, E.; Dellarocca, V.; Maschmeyer, T.; Rey, F.; Coluccia, S.; Thomas, J.M. *Phys. Chem. Chem. Phys.* **1999**, *1*, 585-592.

23. Kosslick, H.; Landmesser, H.; Fricke, R. *J. Chem. Soc., Farad. Trans.* **1997**, *93*, 1849-1854.

24. Bouh, A.O.; Rice, G.L.; Scott, S.L. *J. Am. Chem. Soc.* **1999**, *121*, 7201- .

25. Lin, W.; Frei, H. *J. Am. Chem. Soc.* **2002**, *124*, 9292-9298.

26. Morey, M.S.; O'Brien, S.; Schwarz, S.; Stucky, G.D. *Chem. Mater.* **2000**, *12*, 898- .

27. Nakamura, R.; Frei, H. *J. Am. Chem. Soc.* **2006**, 128, 10668-10669.

28. Moisii, C.; Deguns, E.W.; Lita, A.; Callahan, S.D.; v.d.Burgt, L.J.; Magana, D.; Stiegman, A.E. *Chem. Mater.* **2006**, *18*, 3965-3975.

29. Groppo, E.; Lamberti, C.; Bordiga, S.; Spoto, G.; Zecchina, A. *Chem. Rev.* **2005**, *105*, 115-183.

30. Lever, A.B.P. *Inorganic Electronic Spectroscopy*, 2nd ed.; Elsevier: Amsterdam, 1984; p. 380.

31. Lever, A.B.P. *Inorganic Electronic Spectroscopy*, 2nd ed.; Elsevier: Amsterdam, 1984; p. 397.

32. Zhu, Z.; Chang, Z.; Kevan, L. *J. Phys. Chem. B.* **1999**, *103*, 2680-2688.

33. Yu, J.; Feng, Z.; Xu, L.; Li, M.; Xin, Q.; Liu, Z.; Li, C. *Chem. Mater.* **2001**, *13*, 994-998.

34. Luan, Z.; Meloni, P.A.; Czernuszewicz, R.S.; Kevan, L. *J. Phys. Chem. B* **1997**, *101*, 9046-9051.

35. Zhu, Z.; Hartmann, M.; Maes, E.M.; Czernuszewicz, R.S.; Kevan, L. *J. Phys. Chem. B.* **2000**, *104*, 4690-4698.

36. Weckhuysen, B.M.; Schoonheydt, R.A.; Mabbs, F.E.; Collison, D. *J. Chem. Soc. Faraday Trans.* **1996**, *92*, 2431-2436.

37. *Standard Potentials in Aqueous Solution;* Bard, A.J.; Parsons, R.; Jordan, J.; Marcel Dekker: New York, 1985; p. 461.

38. Verberckmoes, A.A.; Weckhuysen, B.M.; Schoonheydt, R.A. *Microporous Mesoporous Mater.* **1998**, *22*, 165-178.

39. Lever, A.B.P. *Inorganic Electronic Spectroscopy*, 2nd ed.; Elsevier: Amsterdam, 1984; p. 480, 496.

40. Thomson, S.; Luca, V.; Howe, R. *Phys. Chem. Chem. Phys.* **1999**, *1*, 615-619.

41. Weckhuysen, B.M.; Verberckmoes, A.A.; Uytterhoeven, M.G.; Mabbs, F.E.; Collison, D.; de Boer, E.; Schoonheydt, R.A. *J. Phys. Chem. B* **2000**, *104*, 37-42.

42. Diaz, J.F.; Balkus, K.J., Jr.; Bedioui, F.; Kurshev, V.; Kevan, L. *Chem. Mater.* **1997**, *9*, 61-67.

43. Hadjiev, V.G.; Iliev, M.N.; Vergilov, I.V. *J. Phys. C* **1988**, *21*, L199-L201.

44. Blasse, G.; Dirksen, G.J. *J. Solid State Chem.* **1981**, *37*, 390-392.

45. Bi, H.; Cai, W.; Zhang, L. *Mater. Res. Bull.* **2000**, *35*, 1495-1501.

46. Keller, B.; Legendziewicz, J.; Przybylski, J.; Guzik, M.; Glinski, J. *J. Alloys Comp.* **2002**, *341*, 197-202.

47. Reddy, B.M.; Khan, A.; Lakshmanan, P. *J. Phys. Chem. B* **2005**, *109*, 3355-3363.

48. Laha, S.C.; Mukherjee, P.; Sainkar, S.R.; Kumar, R. *J. Catal.* **2002**, *207*, 213-223.

49. Yao, W.; Chen, Y.; Min, L.; Fang, H.; Yan, Z.; Wang, H.; Wang, J. *J. Mol. Catal. A: Chemical* **2006**, *246*, 162-166.

50. Han, H.; Frei, H. *Angew. Chem. Int. Ed.*, submitted.

51. Blasse, G.; Korte, P.H.M.D.; Mackor, A. *J. Inorg. Nucl. Chem.* **1981**, *43*, 1499-1503.

52. Blasse, G. *Struct. Bonding* **1991**, *76*, 153.

53. Pak, C.; Haller, G.L. *Microporous Mesoporous Mater.* **2001**, *48*, 165-170.

54. Babonneau, F.; Doeuff, S.; Leaustic, A.; Sanchez, C.; Cartier, C.; Verdaguer, M. *Inorg. Chem.* **1988**, *27*, 3166.

55. Gibb, T.C. *J. Mater. Chem.* **1992**, *2*, 57-64.

56. Arcon, I.; Mirtic, B.; Kodre, A. *J. Am. Ceram. Soc.* **1998**, *81*, 222-224.

57. Wang, Y.; Ohishi, Y.; Shishido, T.; Zhang, Q.; Yang, W.; Guo, Q.; Wan, H.; Takehira, K. *J. Catal.* **2003**, *220*, 347-357.

58. Oldroyd, R.D.; Sankar, G.; Thomas, J.M.; Ozkaya, D. *J. Phys. Chem. B* **1998**, *102*, 1849-1855.

59. Sham, T.K. *J. Chem. Phys.* **1983**, *79*, 1116-1121.

60. Zhang, J.; Wu, Z.; Liu, T.; Hu, T.; Wu, Z.; Ju, X. *J. Synchrotron Rad.* **2001**, *8*, 531-532.

61. Walker, G.C.; Barbara, P.F.; Doorn, S.K.; Dong, Y.; Hupp, J.T. *J. Phys. Chem.* **1991**, *95*, 5712-5715.

62. Kelly, C.A.; Meyer, G.J. *Coord. Chem. Rev.* **2001**, *211*, 295-311.

63. Khoudiakov, M.; Parise, A.R.; Brunschwig, B.S. *J. Am. Chem. Soc.* **2003**, *125*, 4637-4644.

64. Macpherson, B.P.; Bernhardt, P.V.; Hauser, A.; Pages, S.; Vauthey, E. *Inorg. Chem.* **2005**, *44*, 5530-5536.

Figure Captions

Fig. 1: FT-IR spectra showing the changes of silanol group intensities after reaction of Ce^{III} precursor. Panel (A): (a) Ti-MCM-41 before grafting, (b) TiCe-MCM-41 calcined at 350 ^{o}C. Panel (B): (a) MCM-41 before grafting, (b) Ce-MCM-41 calcined at 350 ^{o}C. Spectra were normalized using the silica overtone bands at 1976, 1867, and 1643 cm^{-1}.

Fig. 2: (A) FT-Raman spectra of Cr-AlMCM-41 and TiCr-AlMCM-41 materials: (a) dehydrated Cr^{VI}-AlMCM-41, (b) hydrated Cr^{VI}-AlMCM-41, (c) as-synthesized TiCr-AlMCM-41, (d) TiCr-AlMCM-41 calcined at 350 °C. The broad absorption at 800 cm^{-1} is due to the symmetric Si-O-Si stretch mode of the silica material. The 974 cm^{-1} growth is assigned to ν(Si-O) of terminal SiOH groups perturbed by the grafted metal centers. (B) FT-IR spectra of (a) dehydrated Cr^{VI}-AlMCM-41, (b) hydrated Cr^{VI}-AlMCM-41, (c) as-synthesized TiCr-AlMCM-41, and (d) TiCr-AlMCM-41 calcined at 350 °C. No bands due to di- or polychromates are observed.

Fig. 3: Diffuse Reflectance UV-Vis spectra of mesoporous materials after 1 hr reaction of Ti^{III} precursor with (a) AlMCM-41. Spectrum (b) shows Cr^{VI}-AlMCM-41 before, spectrum (c) after reaction with Ti^{III}, yielding TiCr-AlMCM-41. The inset shows the 500-800 nm region on an expanded absorption scale.

Fig. 4: X-band EPR spectra (20 K) of Cr^{V} centers (A) and Cr^{III} centers (B) of samples: (a) calcined Cr-AlMCM-41, (b) as-synthesized TiCr-AlMCM-41, (c) TiCr-

AlMCM-41 after calcination at 350 °C. The inset of trace (c) shows the 4-fold amplified $g_{//} = 1.890$ signal for tetrahedrally coordinated Cr^{V}.

Fig. 5: X-band EPR spectra of (a) Co^{II}-MCM41 and (b) $TiCo^{II}$-MCM41 recorded at 20 K.

Fig. 6: Diffuse reflectance spectra of (a) Co-MCM-41, (b) sum of Ti-MCM-41 + Co-MCM-41 spectra, (c) $TiCo^{II}$-MCM-41. Because of the negligible amount of Co^{II} grafted onto plain MCM-41 in the absence of a base, triethylamine was added for the preparation of Co^{II}-MCM-41 (for activating silanol groups, see text). By contrast, no base was used for the synthesis of $TiCo^{II}$-MCM-41. The additional absorption from UV to visible region (extending from 335 nm to approx. 650 nm) of $TiCo^{II}$-MCM-41 is due to MMCT $Co^{II} + Ti^{IV} \rightarrow Co^{III} + Ti^{III}$.

Fig. 7: Diffuse reflectance spectra of (a) Ce^{III}-MCM-41 amplified 6.5-fold (per ICP result, see text) to reflect the absorption of Ce^{III} present in the $TiCe^{III}$-MCM-41 sample; (b) sum of Ti-MCM-41 + (a); (c) $TiCe^{III}$-MCM-41. The additional absorption in the range 350 - 550 nm of $TiCe^{III}$-MCM-41 is due to MMCT $Ce^{III} + Ti^{IV} \rightarrow Ce^{IV} + Ti^{III}$.

Fig. 8: Diffuse reflectance spectra of (a) Cr^{III}-AlMCM-41; (b) sum of Ti-MCM-41 + (a); (c) $TiCr^{III}$-AlMCM-41 prepared by reduction with hydroxylamine. The additional visible absorption (ca. 350 - 600 nm) of $TiCr^{III}$-AlMCM-41 is due to MMCT $Cr^{III} + Ti^{IV} \rightarrow Cr^{IV} + Ti^{III}$. Because the Ti content of the Ti-only material using $Ti^{III}(THF)_3Cl_3$

precursor is negligible, a Ti-AlMCM-41 material using the conventional Ti grafting method was employed to compute spectrum (b).

Fig. 9: Co K-edge XANES spectra of (a) Co^{II}-MCM-41 and (b) $TiCo^{II}$-MCM-41. Panel A shows K-edge and EXAFS region, while panel B gives the pre-edge peak of the two samples on an expanded scale.

Fig. 10: Cr K-edge XANES spectra of (a) calcined Cr^{VI}-AlMCM-41, (b) as-synthesized TiCr-AlMCM-41, (c) calcined TiCr-AlMCM-41, (d) reduced TiCr-ALMCM-41 (using hydroxylamine). Panel A shows the K-edge, panel B the pre-edge region on an expanded scale. Note that in panel B, spectrum (a), the amplitude of the very intense pre-edge peak of Cr^{VI} was reduced by a factor of 10 to facilitate comparison with the spectra (b) through (d).

Fig. 11: Panel A: Cr K-edge EXAFS (χ^3 weighted) FT plots of (a) Cr^{VI}-AlMCM-41, (b) as-synthesized TiCr-AlMCM-41, (c) TiCr-AlMCM-41 calcined at 350 ^oC. Panel B: Cr K-edge EXAFS (χ^3 weighted) FT plots of (a) Cr^{VI}-AlMCM-41, (b) same sample after reduction by hydroxylamine, (c) TiCr-AlMCM-41 reduced by hydroxylamine.

Fig. 12: Panel A: Ce L_3-edge absorption of (a) as-synthesized Ce^{III}-MCM-41, (b) as-synthesized $TiCe^{III}$-MCM-41. Panel B: Same samples calcined at 350 ^oC (a) Ce^{IV}-MCM-41, (b) $TiCe^{IV}$-MCM-41.

Table 1:

Metal precursor	Metal Uptake (in percent)			
	MCM-41	Ti-MCM-41 (Ti/Si =1:100)[d]	Ti-MCM-41 (Ti/Si =3:100)[d]	CrAl-MCM-41 (Cr/Al/Si = 2:3.7:100)[d]
$Co^{II}(CH_3CN)_2Cl_2$ (0.0067 M)	1[a]	12[a]	25[a]	—
$Ce^{III}(NO_3)_3$ (0.0067 M)	9[b]	20[b]	48[b]	—
$Ti^{III}(THF)_3Cl_3$ (0.0134 M)	3[c]	—	—	90[c]

(a) Monitored by the intensity of Co^{II} d-d transition band at 681 nm of supernatant UV-Vis spectra after 2 hr reaction at RT. (b) Monitored by the Ce^{III} charge transfer band at 262 nm in supernatant UV-Vis spectra after 2 hr reaction (1 hr at RT and additional 1 hr at 65 °C). (c) Monitored by the Ti^{III} charge transfer band at 240 nm in supernatant UV-Vis spectra after 1 hr reaction at RT. (d) Ti/Si ratio determined by ICP-MS.

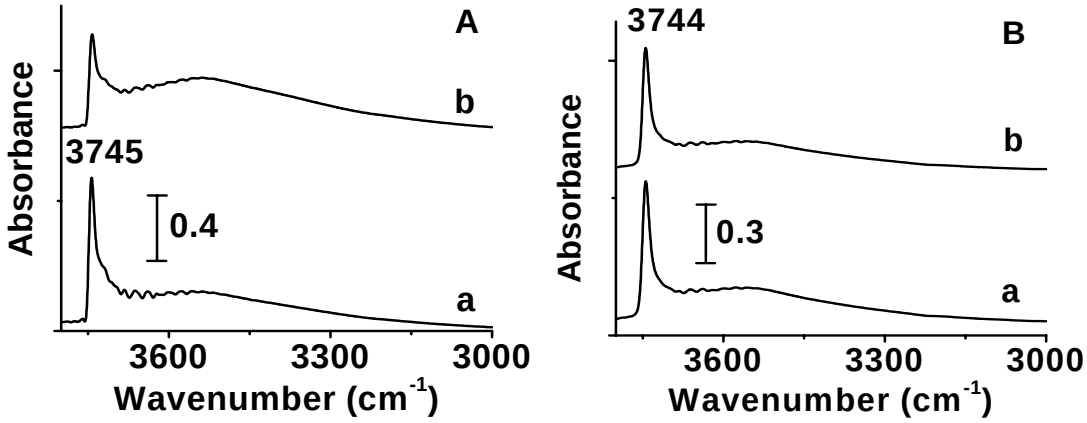
A
b
3745
0.4
a
Absorbance
3600
3300
3000
Wavenumber (cm-1)
3744
B
b
0.3
a
Absorbance
3600
3300
3000
Wavenumber (cm-1)

Fig. 1

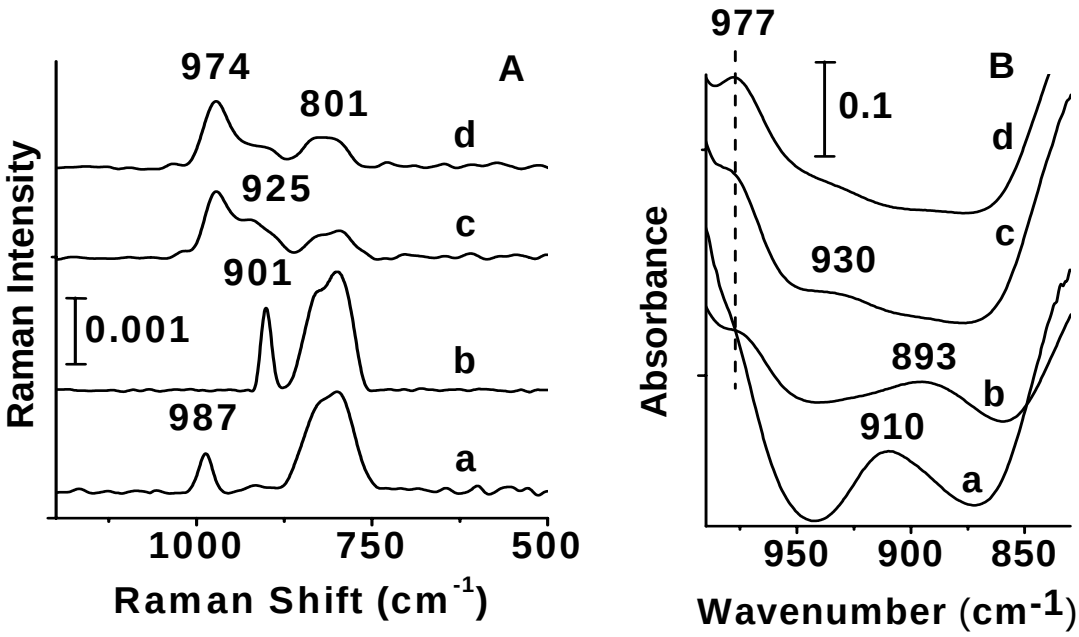
974
801
A
d
925
c
901
0.001
b
987
a
1000
750
500
Raman Shift (cm-1)
Raman Intensity
977
B
0.1
d
c
930
893
b
910
a
950
900
850
Wavenumber (cm-1)
Absorbance

Fig. 2

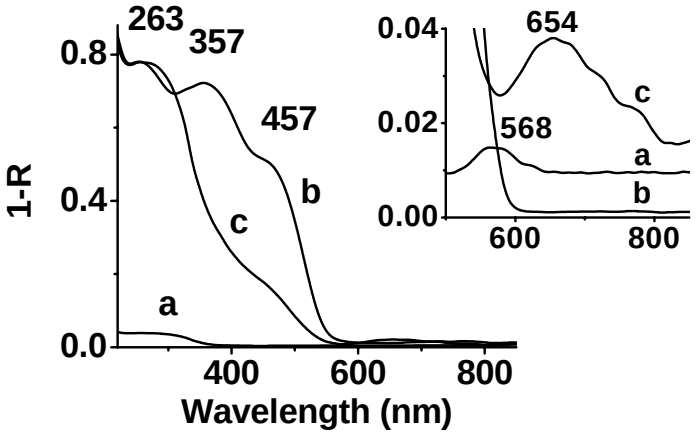
263
357
457
b
c
a
0.8
0.4
0.0
1-R
400
600
800
Wavelength (nm)
654
568
0.04
0.02
0.00
600
800

Fig. 3

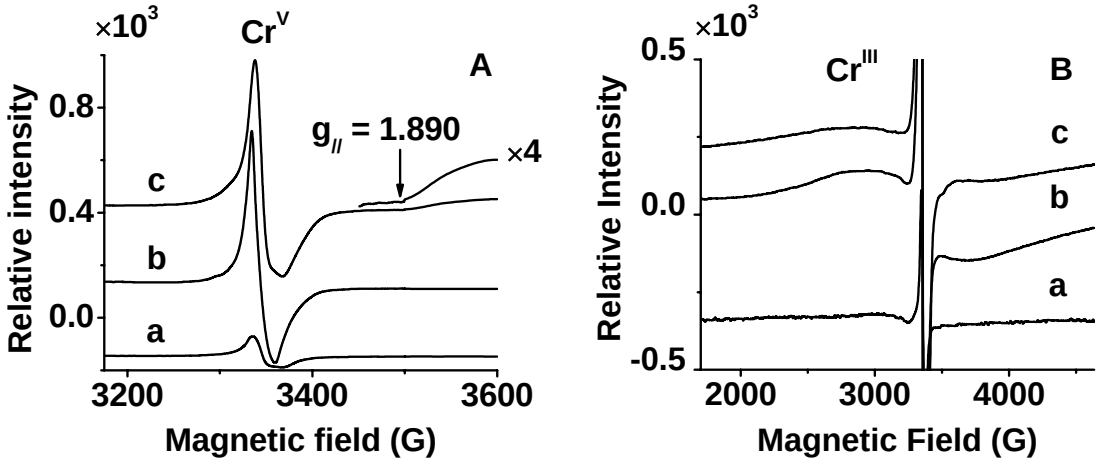
×10^3
Cr^V
A
g// = 1.890
×4
c
b
a
0.8
0.4
0.0
Relative intensity
3200
3400
3600
Magnetic field (G)
×10^3
0.5
Cr^III
B
c
b
a
0.0
-0.5
Relative Intensity
2000
3000
4000
Magnetic Field (G)

Fig. 4

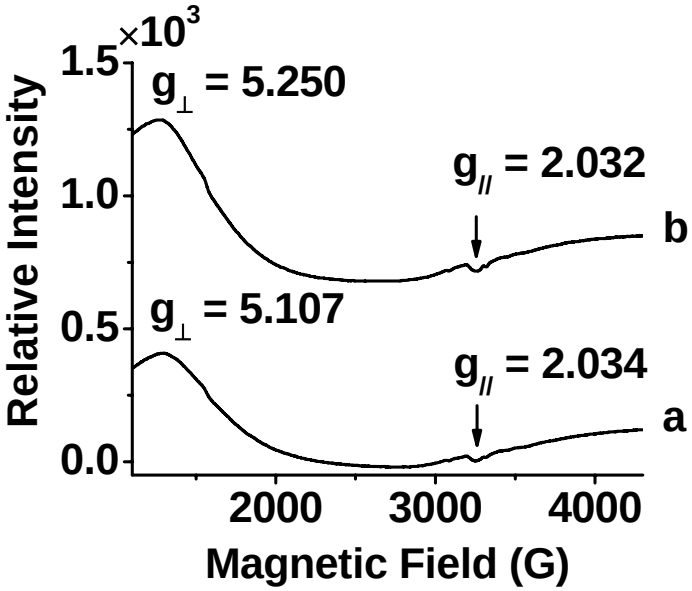
×10^3
1.5
1.0
0.5
0.0
Relative Intensity
g⊥ = 5.250
g// = 2.032
b
g⊥ = 5.107
g// = 2.034
a
2000
3000
4000
Magnetic Field (G)

Fig. 5

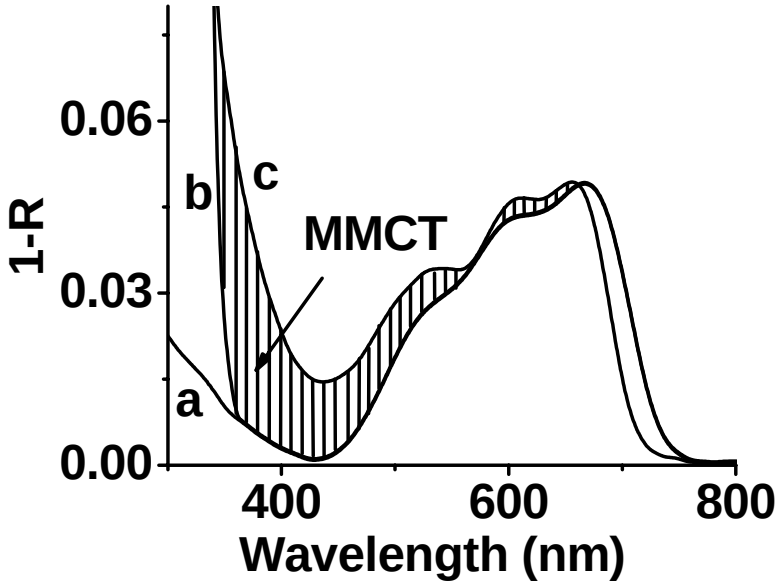

Fig. 6

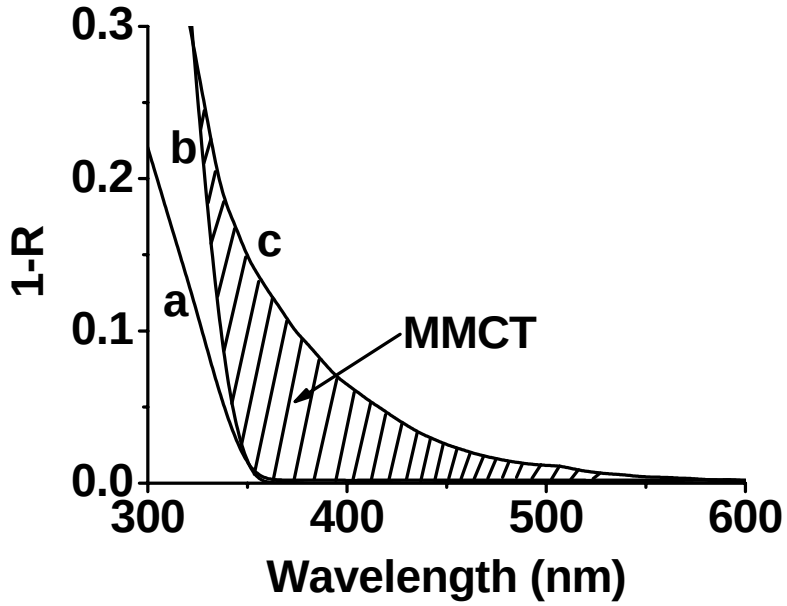

Fig. 7

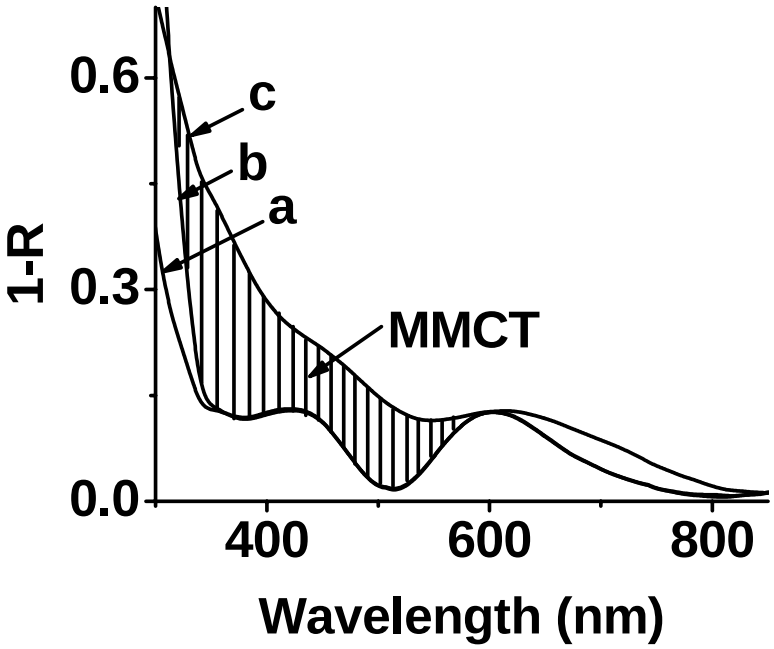

Fig. 8

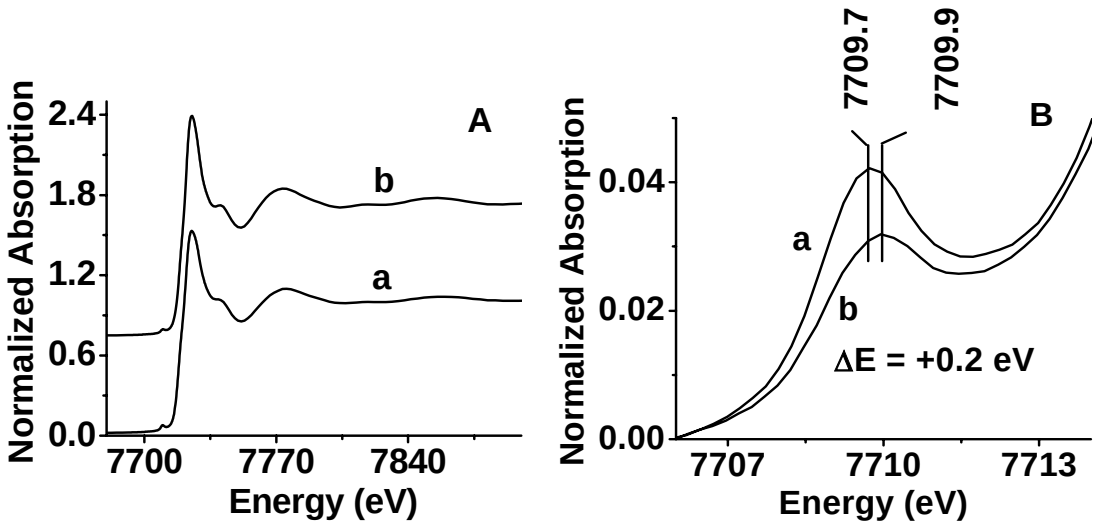
Normalized Absorption
2.4
1.8
1.2
0.6
0.0
A
b
a
7700
7770
7840
Energy (eV)
7709.7
7709.9
B
0.04
0.02
0.00
a
b
ΔE = +0.2 eV
7707
7710
7713
Energy (eV)

Fig. 9

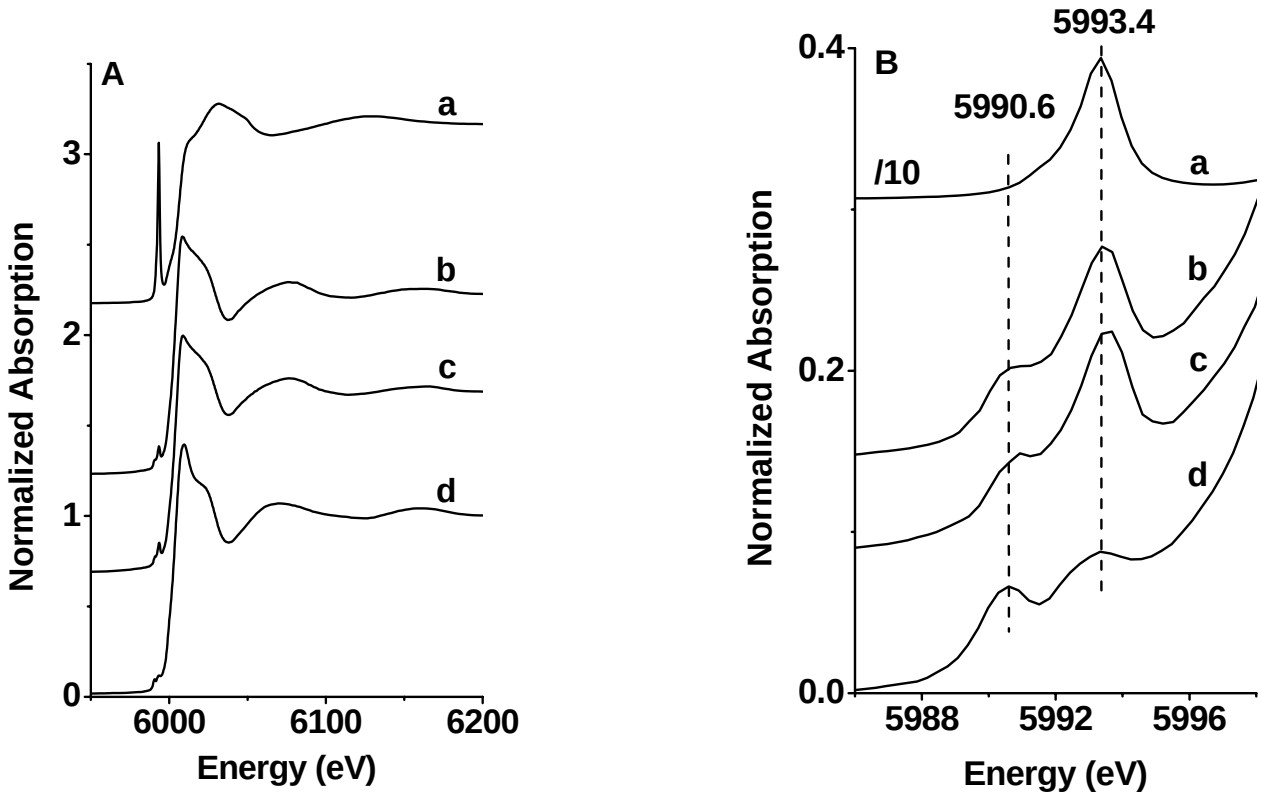
A
a
b
c
d
Normalized Absorption
Energy (eV)
6000
6100
6200
0
1
2
3
B
5993.4
5990.6
/10
0.0
0.2
0.4
5988
5992
5996

Fig. 10

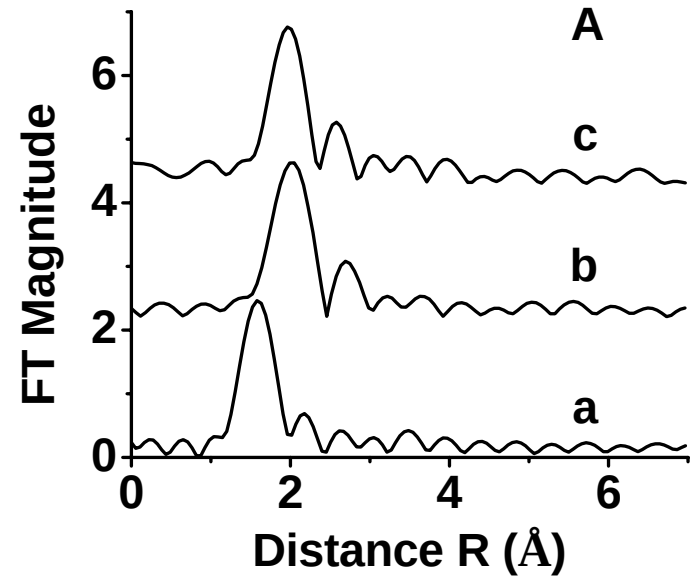
A
c
b
a
FT Magnitude
0
2
4
6
Distance R (Å)

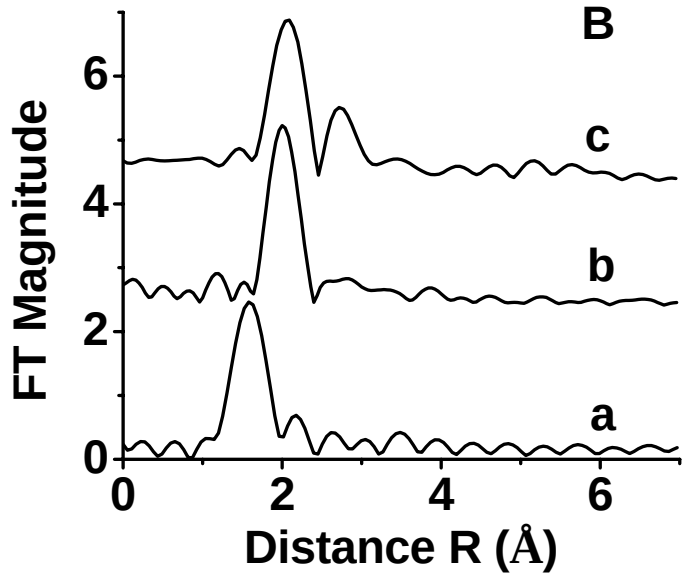
B
c
b
a
FT Magnitude
0
2
4
6
Distance R (Å)

Fig. 11

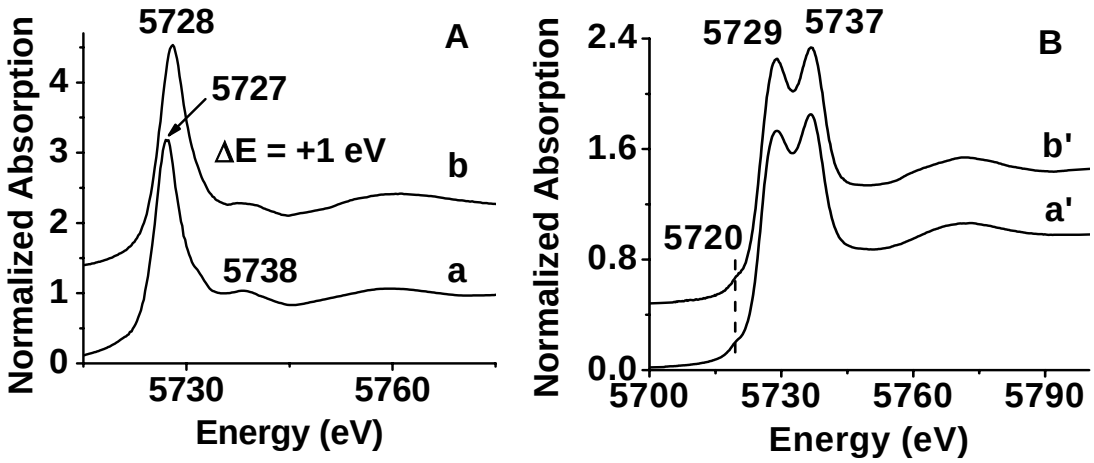
Normalized Absorption
5728
A
5727
ΔE = +1 eV
b
5738
a
0
1
2
3
4
5730
5760
Energy (eV)
Normalized Absorption
2.4
5729
5737
B
b'
a'
1.6
5720
0.8
0.0
5700
5730
5760
5790
Energy (eV)

Fig. 12

Supporting Information

Controlled Assembly of Heterobinuclear Sites on Mesoporous Silica: Visible Light Charge-Transfer Units with Selectable Redox Properties

Hongxian Han and Heinz Frei*

Physical Biosciences Division, Lawrence Berkeley National Laboratory, University of California, Berkeley, CA 94720

E-mail: HMFrei@lbl.gov

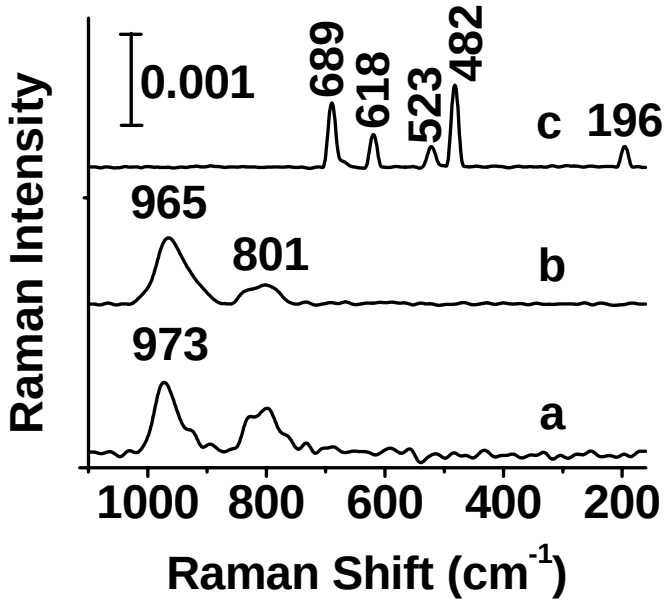

Fig. S1: FT-Raman spectra of (a) Co^{II}-MCM-41 calcined at 350°C; (b) $TiCo^{II}$-MCM-41 calcined at 350°C; and (c) 1%Co_3O_4 mechanically mixed with MCM-41. Co_3O_4 (c) shows distinct Raman absorption bands at 689, 618, 523, 482 and 196 cm^{-1}, which were not observed in Co^{II}-MCM-41 and $TiCo^{II}$-MCM-41 materials. No Co_3O_4 clusters formation indicates that Co^{II} was well dispersed on the surface of nanoporous slica.

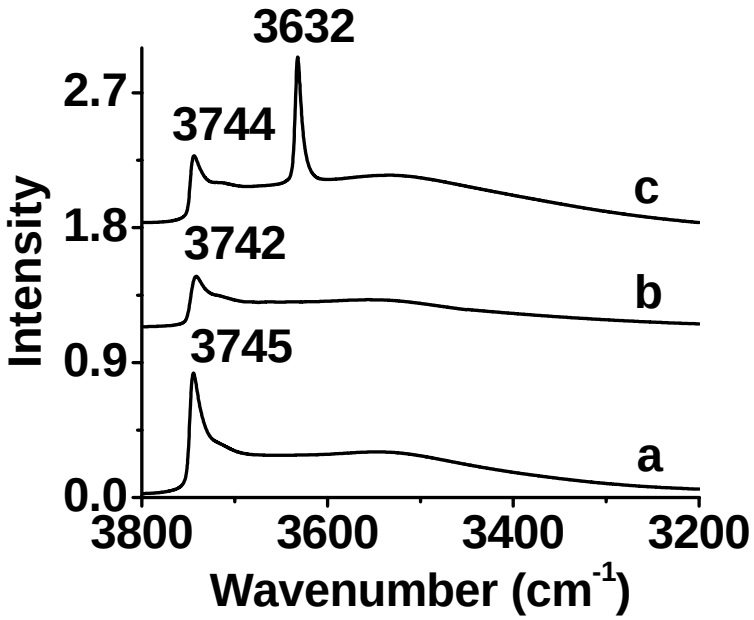

Fig. S2 : FTIR spectra of (a) Co-MCM41; (b) CoTi-MCM41; and (c) $Co(OH)_2$ mechanically mixed with MCM41 (molar ratio Co/Si = 1:100). For reference of FT-IR spectra of $Co(OH)_2$: Hou, Y.; Kondoh, H.; Shimojo, M.; Kogure, T.; Ohta, T., *J. Phys. Chem. B* 2005, 109, 19094-19098.

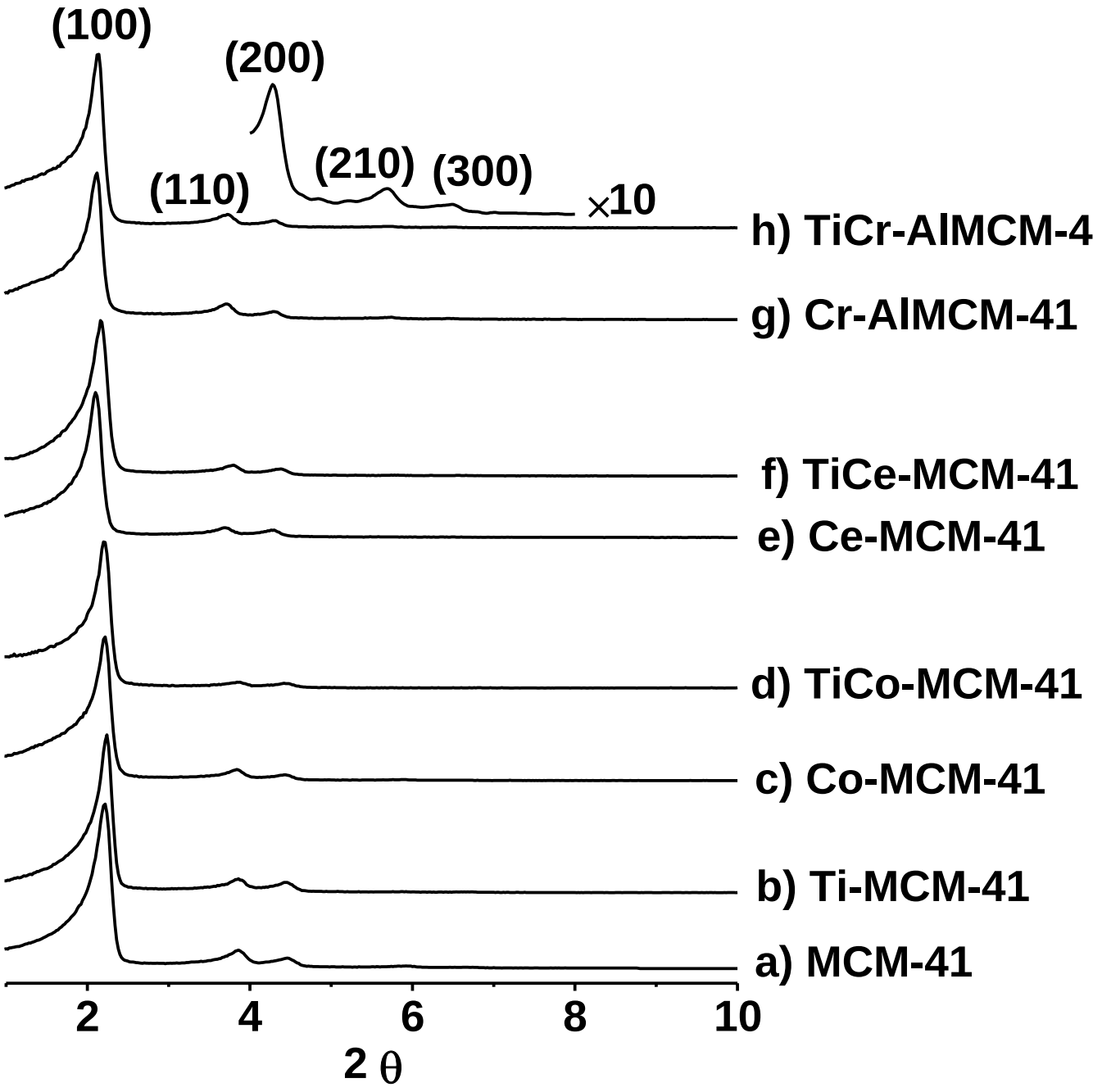

Fig. S3: XRD patterns of the synthesized materials show long range ordering of mesoporous structure by the observation of (100), (110) and (200) Brag reflection peaks.

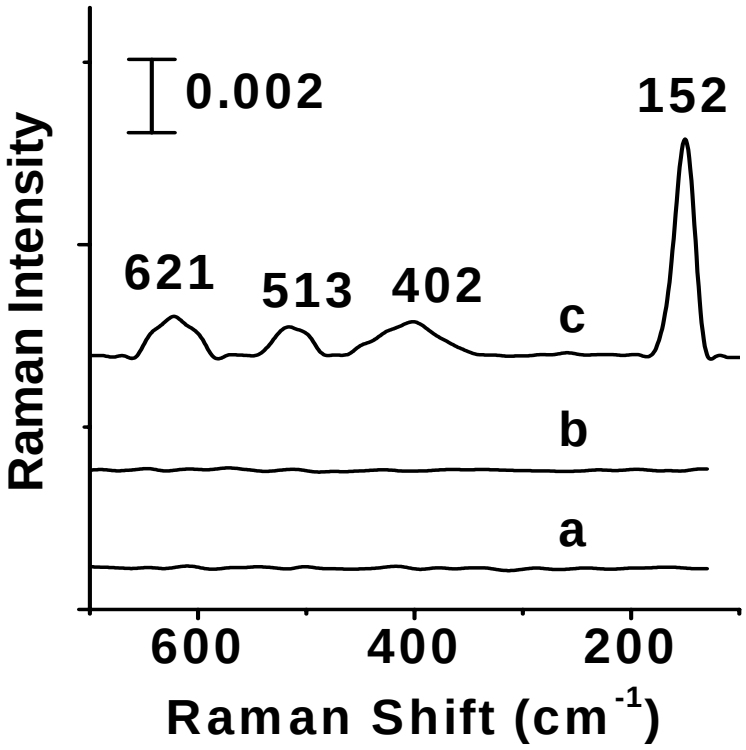

Fig. S4: FT-Raman spectra of (a) as-synthesized TiCr-AlMCM-41; (b) TiCr-AlMCM-41 calcined at 350 ºC; and (c) TiO_2 mechanically mixed with MCM41 (molar ratio Ti/Si = 1:50). For reference of FT-Raman spectra of TiO_2, see: Miller J. M.; Lakshmi, L. J., *J. Phys. Chem. B* 1998, 102, 6465-6470. Cr_2O_3 has a strong characteristic Raman band at ca. 550 cm^{-1}, see ref.: Zuo, J.; Xu C., *J. Raman. Spec.* 1996, 27, 921-923.

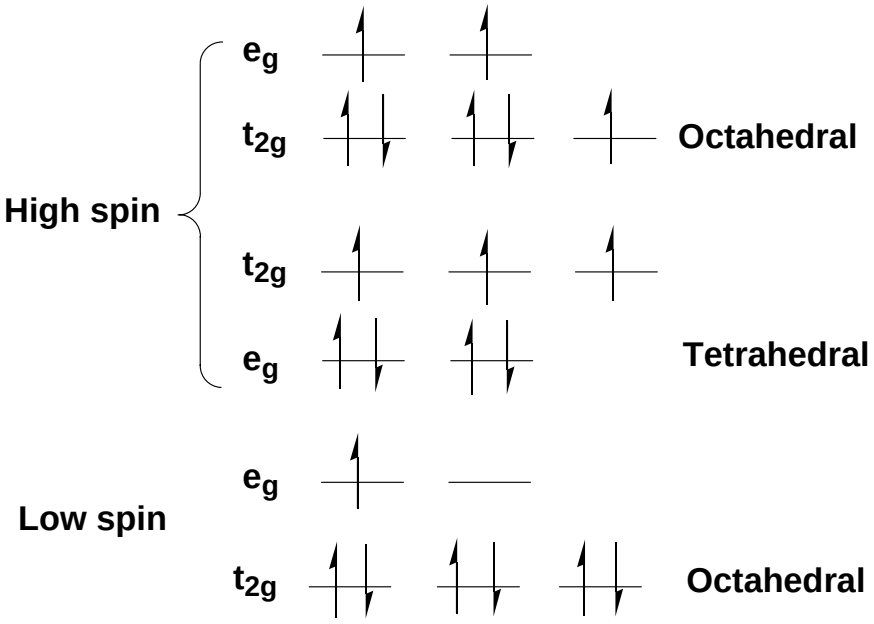

Fig. S5: Electronic configuration of high spin and low spin Co^{II} d-electrons in T_d and O_h coordinations.

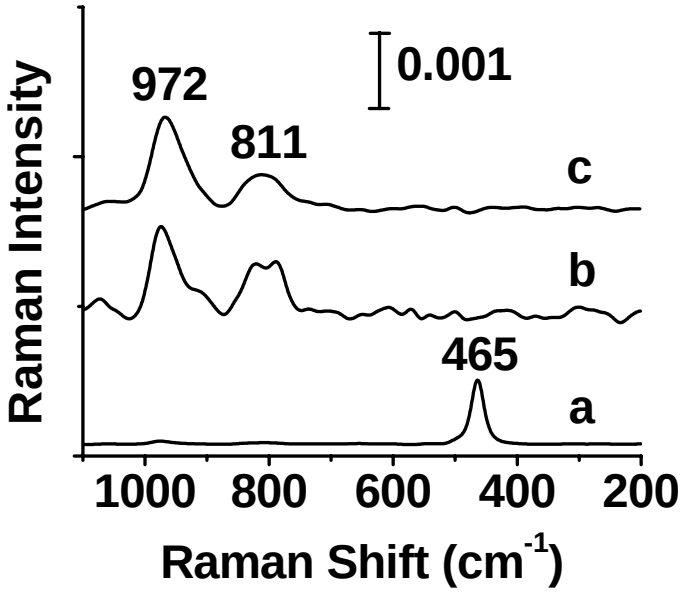

Fig. S6: FT-Raman spectra of (a) 1%CeO_2 mixed with MCM-41; (b) Ce-MCM-41 calcined at 350°C; and (c) TiCe-MCM-41 calcined at 350°C. CeO_2 (a) shows a very

intense Raman absorption at 465 cm^{-1}, which was not observed in Ce-MCM-41 and TiCe-MCM-41. No CeO_2 clustering indicates that Ce^{III} was well dispersed on the surface of nanoporous silica.

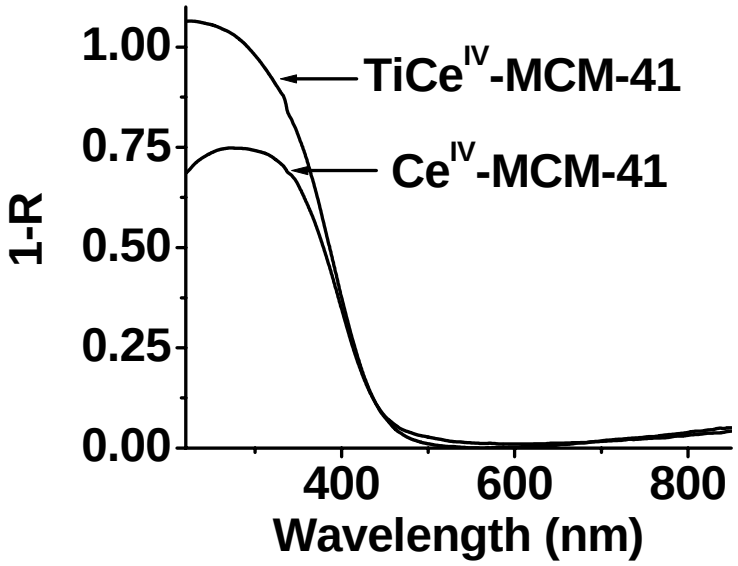

Fig. S7: Diffuse Reflectance UV-Vis spectra of Ce^{IV}-MCM-41 and $TiCe^{IV}$-MCM-41. Both materials were calcined at a mild temperature of 350 °C. MMCT of Ce^{III} to Ti^{IV} is lost due to Ce^{III} oxidation to Ce^{IV} after calcination.